






Redefining the heterogeneity of peripheral nerve cells in health and autoimmunity

Jolien Wolbert^{a,1}, Xiaolin Li^{a,1}, Michael Heming^{a,1} , Anne K. Mausberg^b, Dagmar Akkermann^c, Clara Frydrychowicz^c, Robert Fledrich^d , Linda Groeneweg^e, Christian Schulz^f, Mark Stettner^b, Noelia Alonso Gonzalez^e , Heinz Wiendl^a, Ruth Stassart^{c,2}, and Gerd Meyer zu Hörste^{a,2,3}

^aDepartment of Neurology with Institute of Translational Neurology, University Hospital Münster, Münster 48149, Germany; ^bDepartment of Neurology, University Hospital Essen, University Duisburg Essen, Essen 45147, Germany; ^cDepartment of Neuropathology, University Hospital Leipzig, Leipzig 04103, Germany; ^dInstitute of Anatomy, Leipzig University, Leipzig 04103, Germany; ^eInstitute of Immunology, Westfälische Wilhelms University, Münster 48149, Germany; and ^fMedizinische Klinik und Poliklinik I, Klinikum der Universität München, Ludwig Maximilians Universität, München 81377, Germany

Edited by Lawrence Steinman, Stanford University School of Medicine, Stanford, CA, and approved March 13, 2020 (received for review July 17, 2019)

Peripheral nerves contain axons and their enwrapping glia cells named Schwann cells (SCs) that are either myelinating (mySCs) or nonmyelinating (nmSCs). Our understanding of other cells in the peripheral nervous system (PNS) remains limited. Here, we provide an unbiased single cell transcriptomic characterization of the nondiseased rodent PNS. We identified and independently confirmed markers of previously underappreciated nmSCs and nerve-associated fibroblasts. We also found and characterized two distinct populations of nerve-resident homeostatic myeloid cells that transcriptionally differed from central nervous system microglia. In a model of chronic autoimmune neuritis, homeostatic myeloid cells were outnumbered by infiltrating lymphocytes which modulated the local cell–cell interactome and induced a specific transcriptional response in glia cells. This response was partially shared between the peripheral and central nervous system glia, indicating common immunological features across different parts of the nervous system. Our study thus identifies subtypes and cell-type markers of PNS cells and a partially conserved autoimmunity module induced in glia cells.

transcriptomics | single cell RNA-seq | peripheral nervous system | Schwann cell

The cellular composition of the peripheral nervous system (PNS) appears simple. Neuronal cells are absent and only their specialized cell protrusions termed axons extend into the PNS. Instead, PNS cells are mainly composed of glia cells, that are named Schwann cells (SCs) and morphologically are classified as either myelinating (mySCs) or nonmyelinating (nmSCs). These SCs provide trophic support and electrical insulation to axons partly through the formation of the myelin sheath (1). Myelin is a cell membrane protrusion of SCs that enwraps axons in multiple layers and is required for the rapid conduction of action potentials by axons (2).

While mySCs have been studied in considerable detail, the phenotype of nmSCs and other non-SC cell types, such as fibroblasts and vascular endothelium in the PNS, however, remains poorly defined. Nerve-associated fibroblasts have mostly been defined by morphological characteristics in the PNS, but their function and lineage assignment remain controversial (3). Also, while leukocytes are clearly relevant in inflammatory and traumatic lesions to the PNS (4, 5), their exact composition and phenotype under steady-state conditions remain unknown. Single-cell RNA-sequencing (scRNA-seq) allows defining the cellular composition of complex tissues in an unbiased fashion. However, a single cell characterization of the nondiseased PNS has not been reported and only the transcriptional response to nerve injury has been studied (6). In addition, the cellular response of PNS parenchymal cells to local autoimmune reactions remains unknown (4, 5).

Here, we generated an unbiased cellular map of the healthy PNS at single cell resolution. We identified known and other

markers of mySCs and characterize the composition and marker genes of nmSCs and nerve-associated fibroblasts. We also identified a distinct composition of leukocytes in the PNS including two subsets of tissue-resident homeostatic macrophages. In a mouse model of chronic inflammatory neuropathy, we found that endoneurial lymphocytes preferentially expand and PNS parenchymal cells and their intercellular communication networks respond extensively to autoimmune tissue damage. We found that this reaction to autoimmunity was partially shared between peripheral and central nervous system glia cells, indicating potentially conserved response mechanisms.

Results

Single Cell Transcriptomics Dissects the Cellular Composition of Peripheral Nerves. We aimed to better characterize the cellular composition of the PNS. First, we optimized cell extraction from the PNS and achieved highest cell yield and viability by

Significance

We here present a transcriptional map of peripheral nerve cells in health and autoimmunity. Identified marker genes of non-myelinating Schwann cells and nerve-associated fibroblasts will facilitate a better understanding of the complex cellular architecture of peripheral nerves. The two distinct populations of nerve-resident homeostatic myeloid cells suggest an unexpectedly unique and heterogeneous local immune repertoire in peripheral nerves with signs of heterogeneous ontogenetic origin. Complex changes of local cell–cell communication networks indicate autoimmune neuritis as a disease affecting “immune networks” rather than single cell types. The findings also suggest that immunological features are partially shared and conserved across different parts of the nervous system.

Author contributions: H.W., R.S., and G.M.z.H. designed research; J.W., X.L., A.K.M., D.A., C.F., R.F., L.G., and N.A.G. performed research; C.S., M.S., and N.A.G. contributed new reagents/analytic tools; J.W., X.L., and M.H. analyzed data; J.W., R.S., and G.M.z.H. wrote the paper; C.S. provided Flt3Cre-mT/mG mice; and M.S. provided ICAM-1^{-/-}NOD mice and Lewis rats.

The authors declare no competing interest.

This article is a PNAS Direct Submission.

This open access article is distributed under [Creative Commons Attribution-NonCommercial-NoDerivatives License 4.0 \(CC BY-NC-ND\)](https://creativecommons.org/licenses/by-nc-nd/4.0/).

Data deposition: The raw scRNA-seq data supporting the findings in this study have been deposited in the Gene Expression Omnibus (GEO) repository under accession code [GSE142541](https://www.ncbi.nlm.nih.gov/geo/query/acc.cgi?acc=GSE142541).

¹J.W., X.L., and M.H. contributed equally to this work.

²R.S. and G.M.z.H. contributed equally to this work.

³To whom correspondence may be addressed. Email: gerd.meyerzuhoerste@ukmuenster.de.

This article contains supporting information online at <https://www.pnas.org/lookup/suppl/doi:10.1073/pnas.1912139117/-DCSupplemental>.

First published April 15, 2020.

combining enzymatic digestion (*SI Appendix, Fig. S1A*) with myelin depletion and flow cytometry-based sorting for viable cells (*Methods*) (*SI Appendix, Fig. S1 B and C*). On average, we thereby obtained $1,520 \pm 453$ SD viable cells from the combined brachial plexus and sciatic nerves of one mouse. We then pooled cells from multiple mice ($n = 12$ per batch) and three biological replicates (*SI Appendix, Fig. S1D*) as input for scRNA-seq. After removal of low-quality cells (*Methods*), this returned transcriptional information of 5,400 total high-quality PNS cells, with 596 ± 202 SD average genes detected per cell (*SI Appendix, Table S1*). After normalization (*Methods*), we identified 12 total PNS cell clusters (Fig. 1A).

Overall, 65% of the single cell transcriptomes were assigned to SC and fibroblast cell types, 20% to vascular, and 15% to hematopoietic cell types (Fig. 1B). The unexpectedly high abundance of hematopoietic cells compared to morphological quantification (7) likely reflects their easier extraction and was observed previously (6). One cluster expressed pan-Schwann cell markers (e.g., *ErbB3* and *S100b*) and also coexpressed myelin protein genes (e.g., *Mbp* and *Pmp1*), while another cluster did not express myelin protein genes, but a known SC receptor (*Ngfr/p75*) (Fig. 1C and *SI Appendix, Table S3*). We named these clusters mySCs and nmSCs, respectively (Fig. 1A). An additional cluster expressed fibroblast markers (fibro; *Fn1*, *Fgfr1*, *Col1a*, and *Col3a*) (8). Detection of marker genes in only a proportion of cells of a cluster (Fig. 1D) is inherent to the method (9). Vascular clusters expressed canonical markers of vascular smooth muscle cells (vSMCs; *Acta2*, *Tagln*, and *Tpm2*), of pericytes (PCs; *Rgs5* and *Pdgfrb*), of lymphatic endothelial cells (lymph; *Lyve1* and *Prox1*), and of vascular endothelial cells (EC1s; *Cldn5*, *Egfr1*, and *Pecam1*) (10) (Fig. 1D and *SI Appendix, Table S2*). PCs surround endothelial cells in the vessel wall of the microcirculation (11). An additional endothelial cell cluster expressed genes associated with the blood nerve barrier (EC2s; *Cldn1* and *Slc16a1*) (12). Additional transcripts in the EC2 cluster were either novel to endothelial cells (*Moxd1* and *Nting1*) or had been described in subsets of brain or lung endothelial cells (e.g., *Lypd2*, *Krt19* and *Dleu7*) although EC2s were transcriptionally distinct from brain/lung ECs (10). We thus identify a unique transcriptional phenotype of a subset of PNS endothelial cells.

Four additional clusters expressed pan-hematopoietic markers (e.g., *Ptprc/CD45*) and specifically markers of the myeloid cell lineage (MC; *Lyz2*), macrophages (MP; *Cd68*), T cells (TCs; *Cd3e*), and B cells (BCs; *Cd79*) (Fig. 1D and *SI Appendix, Table S2*) (9). Blood contamination is unlikely, because mice were intracardially perfused and red blood cells (expressing *Hba* and *Hbb*) were absent. We thus define the heterogeneity and provide a census of PNS cells.

To relate our dataset with human diseases, we plotted the average expression of genes associated with hereditary neuropathies against the cell clusters (*SI Appendix, Fig. S2A*). We found that—except for myelin protein genes—most neuropathy genes were preferentially expressed in non-SC cell types (*SI Appendix, Fig. S2A*), suggesting a potential relevance of nonglia cell types in inherited PNS disorders. Notably, neuronal cells are not included in our dataset, which may exaggerate the role of these genes in nonglia cells.

Detailed Transcriptomic Characterization of Schwann Cell and Fibroblast Clusters. Next, we characterized selected clusters in greater detail. The mySC cluster expressed genes encoding PNS myelin proteins (*Pmp1*, *Mbp*, and *Mpz*), a key SC lineage transcription factor (*Sox10*), and other regulators of myelination (e.g., *Ptm* and *Cryab*) (13) (Fig. 1C and D). In addition, genes highly expressed in mySCs were associated with lipid metabolism (e.g., *Apoe* and *Dbi1*) (14) and STAT3 (*Socs3*) (15) signaling pathways (*SI Appendix, Tables S2 and S3*). Expression of JNK

pathway genes (*Fos* and *Junb*) (16) in mySCs (*SI Appendix, Fig. S3A*) has been described (17), but could represent immediate early gene expression resulting from digestion. Gene set enrichment analysis (GSEA) replicated enrichment of signaling pathways (e.g., TGF β /SMAD) previously associated with Schwann cell function (*SI Appendix, Table S5*). We next screened for transcripts not previously described in mySCs or in PNS myelination (*SI Appendix, Table S4*). Such “new-in-mySC” transcripts included metallothioneins (*Mt1* and *Mt2*) and a ferritin chain gene (*Fth1*) with metal transport and antioxidant functions and unknown relevance in the PNS (18). Also, the transcription factor *Btg2* was not previously described in mySCs. We thus identified candidate genes in mySCs (*SI Appendix, Fig. S3A*).

Next, we further analyzed the nmSC cluster. It highly transcribed a lipoprotein gene (*Apod*) (Fig. 1D and E and *SI Appendix, Table S2*), that is known to be expressed in the PNS (19) in Schwann cells (20) with functions in SC–macrophage communication and promoting axonal regeneration (21, 22). The nmSC cluster also expressed ceruloplasmin (*Cp*) involved in copper metabolism and reported as a potential pan-SC marker (23). When we focused on receptors (Panther class: PC00197) we found that expression of the genes *Man2*, *Myoc*, *Hspg2/Perlecan*, *Col6a*, and *Lama2* in nmSCs was in accordance with their known expression and/or function in the PNS (24–27) (*SI Appendix, Fig. S3B*). Among transcription factors (TFs) (Panther class: PC00218), expression and/or function of *Tcf4*, *Spry2*, and *Cebpd* have been described in SCs (28–30) (*SI Appendix, Fig. S3B*). Overall, this supports the assignment of the nmSC cluster to the SC lineage.

Coexpression of *Ngfr/p75*, *Cspg4/NG2*, and *Pdgfr/PDGFR β* was previously described in novel pericyte-like cells in the PNS (7). We found coexpression of *Ngfr/Cspg4/Pdgfr* in both the nmSC and PC clusters (*SI Appendix, Fig. S3C*).

In addition to these known transcripts, we identified a profile of the nmSC cluster that was distinct from mySCs and included specific cell surface molecules (e.g., *Ccl11* implicated in central nervous system [CNS] myelination) (31), proteases (*Mmp2*), and the TF *Osr2* not previously reported in glia cells (*SI Appendix, Fig. S3B and Table S3*). *Osr2* regulates embryonic mesenchymal cell differentiation (32). GSEA of nmSC marker genes identified pathways related to bone formation (e.g., WP1270 WikiPathway) and neural crest formation (*Tcf4* and *Sox9*) (*SI Appendix, Table S6*). Notably, some TFs that have been implicated in myelination (*Tcf4*, *Spry2*, and *Ebf1*) (33, 34) were expressed in nmSCs at a higher level than in mySCs (*SI Appendix, Fig. S3B*).

The fibro cluster expressed a variety of extracellular matrix (ECM) components (*Dpt* and *Gsn*) including specific collagen genes (*Col1a1*, *Col1a2*, *Col3a1*, and *Col14a1*) (Fig. 1D and *SI Appendix, Table S2*). GSEA accordingly identified pathways associated with ECM formation (*SI Appendix, Table S7*). The cluster also expressed marker genes (*Pi16*, *Clec3b*, and *Cygb*) and TFs (*Prrx1* and *Aebp1*) (Fig. 1E and *SI Appendix, Table S2*), that were previously identified in matrix fibroblasts (8). This supports the idea that the fibro cluster represents nerve-associated fibroblasts (3) with a specific matrix fibroblast phenotype. In this cluster we newly identified *Sfrp4*—a known regulator of the Wnt signaling pathway (35) (Fig. 1D and E and *SI Appendix, Table S2*)—and multiple members of the IGF signaling pathway (*Igfbp6*, *Igfbp4*, and *Igfbp5*) and a single complement component (C3) that is known to inhibit axonal outgrowth (36). This suggests that nerve-associated fibroblasts could coregulate axonal growth.

In conclusion, we identify a previously unknown transcriptional signature and candidate regulators of nmSCs and nerve-associated fibroblasts.

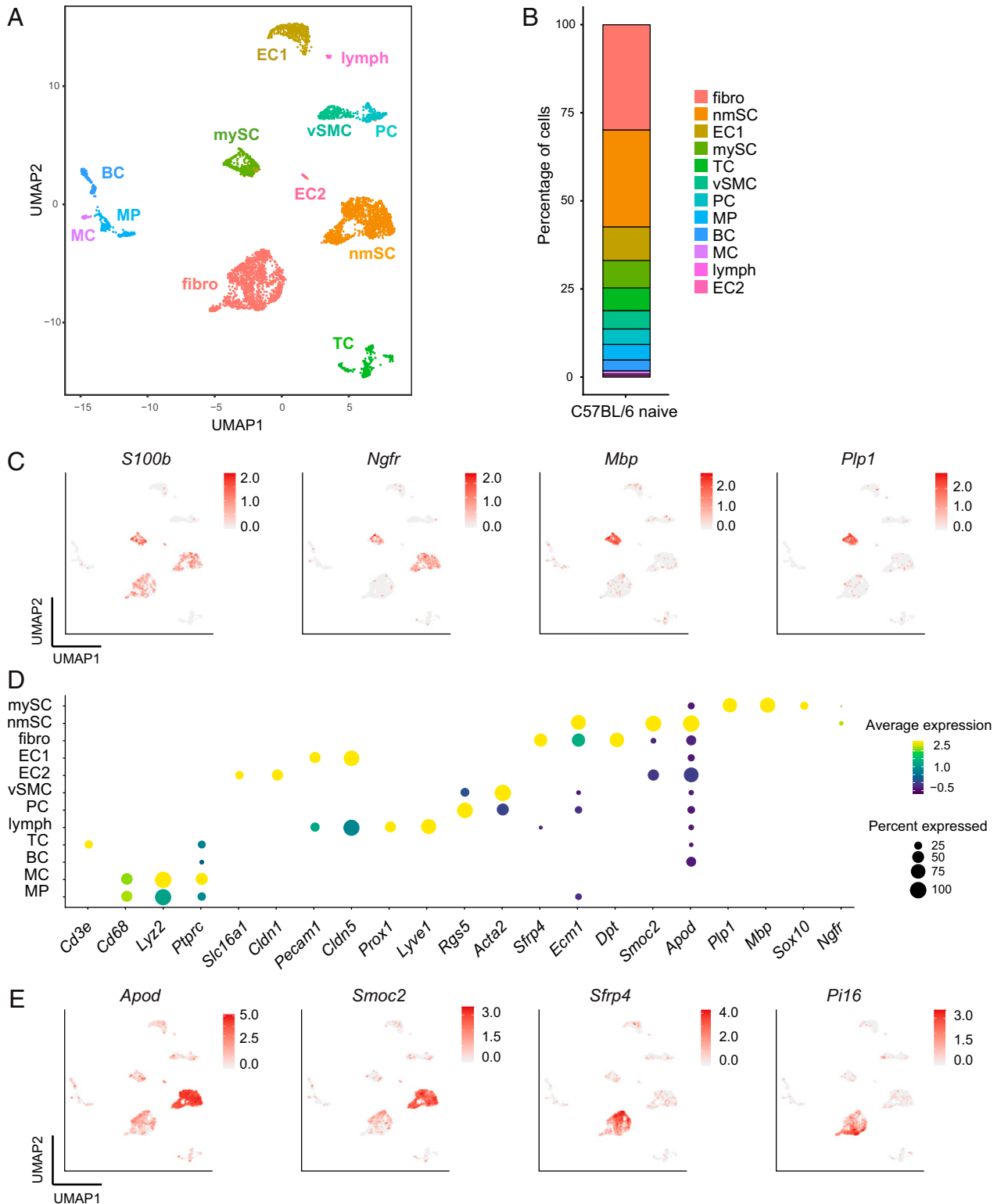


Fig. 1. Single cell transcriptomics defines cellular phenotypes in the mouse PNS. (A) After multistep purification of peripheral nerve cells, 5,400 total single cell (sc) transcriptomes were generated from adult naive female C57BL/6 mice (three biological replicates, $n = 12$ mice each, $n = 36$ total mice), using microfluidics-based scRNA-sequencing. The sc transcriptomes were clustered (*Methods*) and manually annotated to cell types based on marker gene expression. Each dot indicates one cell and clusters are color coded. (B) The proportion of cells in each cluster is depicted. (C) Feature plots of selected marker genes of the SC lineage. Intensity of red indicates expression level. (D) Dotplot of selected marker genes grouped by cluster. The average gene expression level per cluster is color coded and circle size represents the percentage of cells expressing the gene. Threshold was set to a minimum of 10% of cells in the cluster expressing the gene. (E) Feature plots of genes expressed by the nmSC and fibro clusters.

Confirming Lineage Assignment and Expression of nmSC Markers. We next aimed to confirm and localize cell-type markers combining immunohistochemistry (IHC) and RNA in situ hybridization (ISH). From the top genes identified in the nmSC cell cluster (*SI Appendix, Table S2*), we selected transcripts with high and specific expression in the nmSC cluster (*Apod* and *Smoc2*) (Fig. 1 *D* and *E*) and stained them using ISH. *Mbp* was used as positive control of mySCs and showed widespread endoneurial expression (Fig. 2*A*). As expected, the staining pattern of *Mbp* protein and *Mbp* RNA differ (Fig. 2*A* vs. Fig. 2 *C* and *E*). The ISH signal of *Apod* was located solely endoneurially in either large perinuclear aggregates (4.4% of all endoneurial nuclei) or small cytosolic patches (16.9% of all nuclei) (Fig. 2*A*). *Smoc2* was mainly located endoneurially with a similar aggregated morphology (50.9% of all nuclei) (Fig. 2*A*). Partially epineurial staining of *Smoc2* (Fig. 2*A*) was not reproduced in costainings (Fig. 2*B*) and is thus likely unspecific. Cells expressing either of the two markers appeared morphologically distinct from mySCs and also did not express *Mbp* (Fig. 2*A* and *C*).

We next aimed to assign the lineage identity of the nmSC cluster. We therefore costained markers of the nmSC cluster (*Apod* and *Smoc2*) with three known SC lineage markers (*Ngfr*, *S100b*, and *Sox10*) (Fig. 2*B* and *SI Appendix, Figs. S4–S6*). As expected for mRNA (Fig. 1 *C* and *D*), only a proportion of *Apod*⁺ and *Apod*⁺*Smoc2*⁺ cells stained positively for *Ngfr* (36.1 ± 9.5%), *S100b* (57.6 ± 8.5%), or *Sox10* (53.9 ± 5.4%) (Fig. 2*B* and *SI Appendix, Fig. S3D*). We also used a reporter mouse line to identify the glia cell marker *Gfap* on protein level (*Methods*). Both *Apod* and *Smoc2* costained with the four aforementioned lineage markers (Fig. 2*B* and *SI Appendix, Figs. S4–S6*), but not with the mySC marker *Mbp* (Fig. 2*C*), and also not with fibro markers *Vim* (*SI Appendix, Fig. S7A*) and *Pdgfra* (*SI Appendix, Fig. S7B*). This supports the idea that *Apod/Smoc2*-expressing cells in fact represent nmSCs.

Confirming Lineage Assignment and Expression of Fibroblast Markers. We next aimed to confirm and localize selected fibro cluster marker genes (Fig. 1*E*). RNA ISH of *Sfrp4* showed expression in some large epineurial cells with patchy cytosolic staining pattern (Fig. 2*A*). In addition, *Sfrp4* was expressed by small endoneurial cells (5.7% of all nuclei). This supports the idea that the fibro cluster represents endo- and epineurial fibroblasts.

We then first performed costaining of the fibro cluster markers *Sfrp4* and *Pi16* and found that both transcripts colocalized to individual cells (Fig. 2*D* and *SI Appendix, Fig. S7C*). To verify the fibro cluster's lineage assignment, we combined *Pi16* and *Sfrp4* staining with a reporter mouse (*Methods*) and detected colocalization of *Pi16* and *Sfrp4* with *Pdgfra*-driven green fluorescent protein (GFP) in the epineurium (Fig. 2*D* and *SI Appendix, Fig. S8A* and *B*). In contrast, the transcript *Sfrp4* did not contain with either *Sox10* or *Mbp* (Fig. 2 *D* and *E*). This supports the idea that the fibro cluster indeed represents nerve-associated fibroblasts and is distinct from nmSCs and mySCs.

PNS Leukocytes Are Distinct and Contain Unique Homeostatic Macrophages. The abundance (15%) of PNS-resident leukocytes in nondiseased mice was surprising and we therefore characterized them in greater detail. Leukocyte clusters separated into T/NK cell (TC), B cell (BC), macrophage (MP), and myeloid cell (MC) lineage clusters (Fig. 3*A*). The TC cluster (*Cd3e* and *Cd3d*) expressed markers of both the helper T cell (*Il7r*) and cytotoxic (*Cd8a* and *Cd8b1*) subsets (Fig. 3*B*). T cell subsets and natural killer (NK) cells (*Klrd1*, *Klrg1*, and *Nkg7*) did not separate into subclusters due to their low total cell number (Fig. 3*B*). The BC cluster (*Cd79a* and *Ms4a1/Cd20*) expressed markers of naive, nonclass-switched B cells (*Ighd*, negative for: *Xbp1*, *Sdc1/Cd138*) and genes associated with antigen presentation (e.g., *H2-Aa*)

(Fig. 3*B*). Flow cytometry confirmed this overall composition of leukocytes in the murine PNS and indicated the presence of myeloid lineage cells with differing levels of MHC class II expression (two peaks in Fig. 3*C*). This is in line with two distinct tissue resident macrophage populations that are distinguished based on their MHC class II expression (37).

We next tested whether our findings could be confirmed in humans. We therefore stained our sural nerve biopsies of patients without signs of PNS pathology (*SI Appendix, Fig. S9A*). SOX10 (*SI Appendix, Fig. S9B*) and MBP protein (*SI Appendix, Fig. S9C*) served as markers of SCs and mySCs, respectively, while CD34 and ACTA2 are established markers for fibroblasts and vSMC/PCs (*SI Appendix, Fig. S9D* and *E*). Staining for CD45 was used to show the presence of leukocytes (*SI Appendix, Fig. S9F*), while CD68 specifically stained for macrophages (*SI Appendix, Fig. S9G*) and CD4/CD8 for T cell subsets (*SI Appendix, Fig. S9H* and *I*). Endoneurial T cells and macrophages were rare, but clearly identifiable, corresponding to the results in naive mice. We were unable to detect BCs in the nondiseased human PNS. The overall composition of endoneurial leukocytes is thus conserved in human PNS.

We next aimed to better understand the potential heterogeneity of myeloid lineage cells in the murine PNS. In our transcriptional data, we identified two myeloid clusters (*Lyz1* and *Lyz2*) that we named MC and MP (Fig. 3*A*). The MC cluster expressed markers of nonclassical monocytes (*Fcgr3/CD16*) and genes associated with long-lived CNS microglia (*Cx3cr1*) (38), activation (*Csf1r*), phagocytosis (*Cd300a*), and pattern recognition (*Clec4e*) (*SI Appendix, Table S2*).

The MP cluster (*Adgre1/F4/80*) expressed markers of classical monocytes (*Cd14*), nervous system-resident macrophages (*Aif1/Iba1*), and unique chemokines (e.g., *Ccl6*, *Ccl9*, and *Ccl4*) (*SI Appendix, Table S2*). In addition, the MP cluster expressed *Pf4/Cxcl4* (Fig. 3*B*) previously described in blood megakaryocytes (9) and some tissue-resident macrophages (39). PNS leukocytes did not resemble megakaryocytes in cytopins (*SI Appendix, Fig. S10A*) and did not express megakaryocyte markers by flow cytometry (*SI Appendix, Fig. S10B*). Instead, we found that rare small endoneurial cells expressed *Pf4* by ISH (Fig. 3*D*). *Cx3cr1* and *Pf4/Cxcl4* thus identify two distinct subsets of nerve-associated myeloid cells, but not megakaryocytes.

Leukocyte Enrichment Confirms Two Distinct Nerve-Associated Macrophage Populations. Low cell numbers prohibited studying nerve-associated leukocytes in greater detail. We therefore used leukocyte enrichment and rats as donor animals (*Methods*) before subjecting cells to scRNA-seq. We thereby obtained 12,500 total single cell transcriptomes from the rat PNS (*SI Appendix, Table S1*) out of which 35.3% expressed hematopoietic markers (*Ptprc/Cd45*) (Fig. 3*E*). Cell-type identification was again based on marker gene expression (*SI Appendix, Table S8*).

The dataset contained residual nonleukocyte cells which we removed from further analysis (colored in gray in Fig. 3*E*). Leukocyte transcriptomes separated into TCs (*Cd3e* and *Cd2*), BCs (*Cd79a* and *Ighm*), and a small cluster of mast cells (*Cma1* and *Mcpt8*) (Fig. 3 *F* and *G*). The abundant myeloid lineage cells (*Lyz2*) separated into two apparent clusters (Fig. 3 *F* and *G*). One cluster (MPs) expressed features of classical monocytes (*Cd14* and *Ms4a7*), tissue resident macrophages including markers we had identified in mice (*Pf4/Cxcl4* and *Adgre1/F4/80*), complement components (e.g., *C1qb*), and specific chemokines (*Ccl4*, *Ccl3*, and *Cxcl2*) (*SI Appendix, Fig. S10C*). The second cluster (MC) expressed high levels of antigen-presenting molecules (e.g., *RT1-Bb*) and alternative trafficking molecules (*Ccl17*, *Ccl6*, and *Alcam*) (*SI Appendix, Fig. S10C*). Expression of *Cx3cr1* was barely detectable (*SI Appendix, Fig. S10C*). This again supports that the PNS is populated by two subsets of nerve-associated homeostatic myeloid cells.

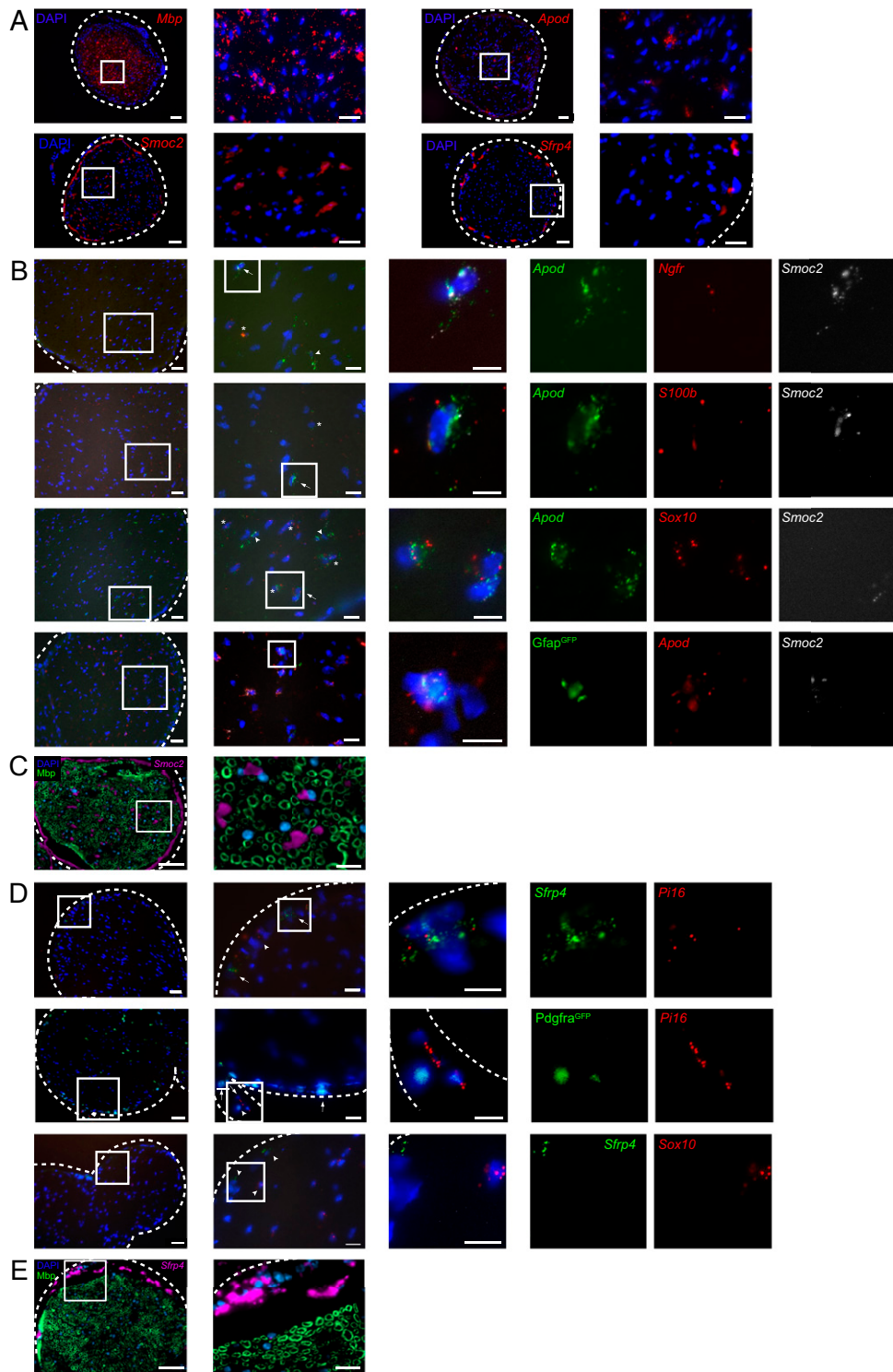


Fig. 2. Localization and lineage assignment of marker genes in the PNS. (A) Paraformaldehyde (PFA)-fixed cryosections of sciatic nerves of naive adult C57BL/6 mice were stained for *Mbp* using RNA ISH. Corresponding ISH stainings of *Apod*, *Smoc2*, and *Sfrp4* are shown with overview (Left) and zoomed (Right) images for each staining. *Mbp* and *Apod* were detected with the ViewRNA ISH Tissue Assay Kit (1-plex) (Thermo Fisher). *Smoc2* and *Sfrp4* were detected with the BaseScope Detection Reagent Kit-RED (ACDbiotech). (B) Fresh-frozen sections of sciatic nerves of naive adult C57BL/6 mice were stained for *Apod*, *Smoc2* together with Schwann cell markers *Ngfr*, *S100b*, and *Sox10* by the multiplex ViewRNA Cell Assay Kit. *SI Appendix, Fig. S1–S3* show additional corresponding stainings. Nerves from *Gfap*^{GFP} mice were costained for *Apod* and *Smoc2* with ISH. (C) PFA-fixed paraffin-embedded sciatic nerves of naive adult C57BL/6 mice were stained for *Smoc2* with the BaseScope Detection Reagent Kit-RED, together with an antibody against *Mbp*. (D) Sections as in B were costained for *Sfrp4* and *Pi16*, and for *Sfrp4* with *Sox10* to show absence of costain. Nerves from *PDGFRα*^{GFP} reporter mice were costained for *Pi16* by the multiplex ViewRNA Cell Assay Kit. *SI Appendix, Fig. S4–S6* show more corresponding stainings. (E) Sections as in C were stained for *Sfrp4* with the BaseScope Detection Reagent Kit-RED together with an antibody against *Mbp*. White dotted line shows the epineurium border of the sciatic nerve. Nuclei were stained with DAPI. (Scale bars: 50 μm, Left; 20 μm, Right; and 10 μm, magnification.) Please note that each dot represents one single RNA molecule. Arrows indicate costaining of all markers, asterisks indicate costain of an identified marker with a known lineage marker, and arrowheads indicate individual staining.

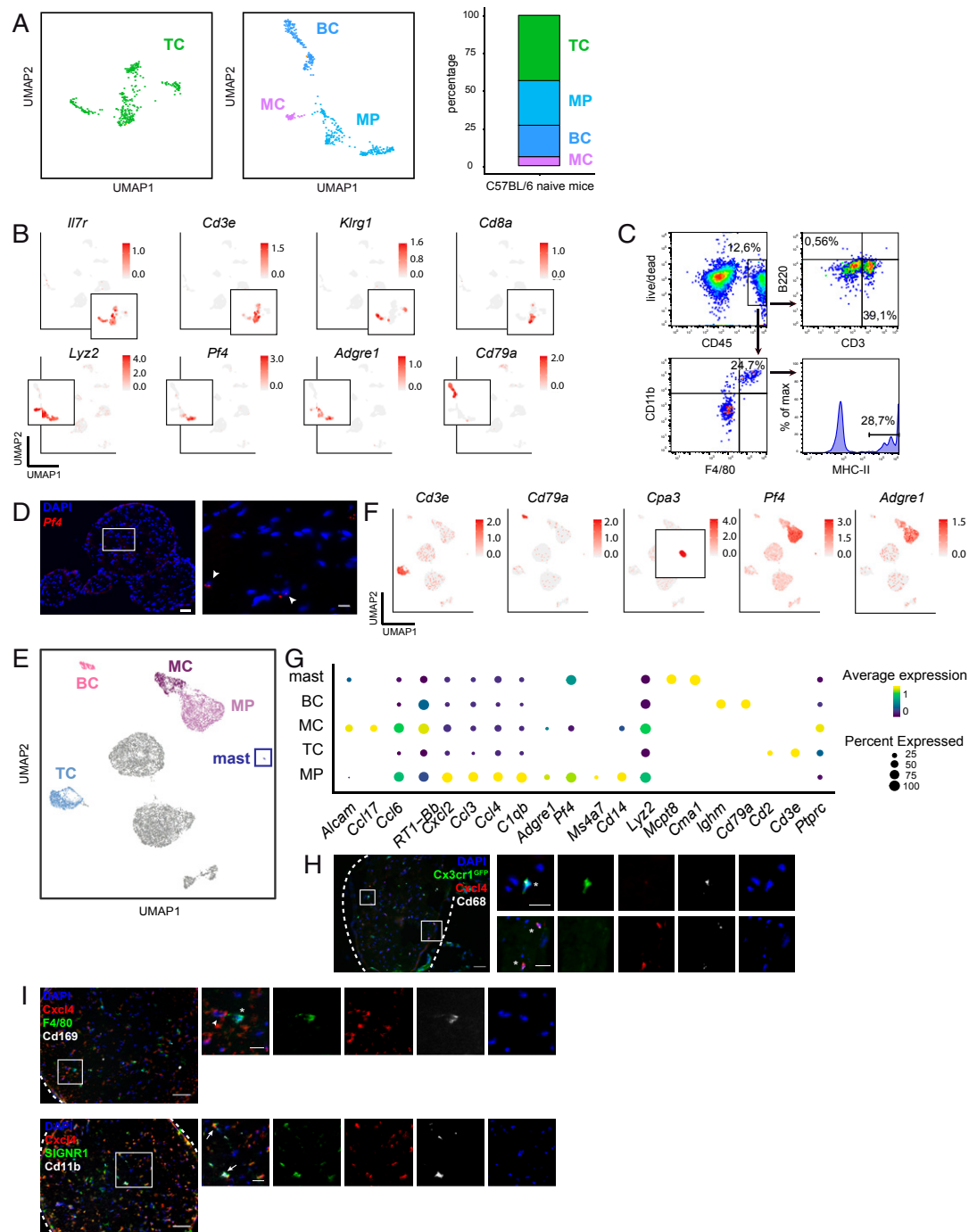


Fig. 3. The composition and phenotype of PNS leukocytes is unique and contains specific macrophage populations. (A) The latent space areas of cell clusters identified as hematopoietic cells in Fig. 1 are depicted in a higher magnification UMAP plot. The proportion of leukocyte subsets is depicted. (B) Feature plots of key leukocyte subset markers are depicted. *Insets* show higher magnification of smaller clusters of interest. *Adgre1* encodes F4/80. Intensity of red indicates expression level. (C) Peripheral nerve cells were purified from two female C57BL/6 mice, pooled, and analyzed by flow cytometry after staining for leukocyte markers. The gating strategy is indicated. The proportion of viable CD45⁺CD11b⁺F4/80⁺ macrophages expressing MHC class II was quantified. One representative out of three independent experiments is shown. (D) Paraformaldehyde fixed cryosections of sciatic nerves of naive female adult C57BL/6 mice were stained for *Pf4* using RNA ISH. The tissue was stained with the 1-plex ViewRNA ISH Tissue Assay Kit (Thermo Fisher). (Scale bars: 50 μ m, *Left* and 10 μ m, *Right*.) (E) Peripheral nerve cells purified from $n = 10$ female Lewis rats were enriched for leukocytes using gradient centrifugation (*Methods*), and processed by scRNA-seq. The resulting 12,500 total rat sc transcriptomes were clustered and the corresponding UMAP plot is shown. Nonhematopoietic cell clusters (*Ptprc*/CD45 negative) are colored in gray to deemphasize. (F) Feature plots showing selected leukocyte markers in the latent space as in E. Intensity of red indicates expression level. (G) Dotplot of selected marker genes of leukocyte clusters. Average expression level per cluster is color coded and circle size represents the percentage of cells expressing the gene. Threshold was set to a minimum of 10% of cells in the cluster expressing the gene. (H) Sciatic nerves from CX3CR1-GFP reporter mice were processed as in D and stained for *Cxcl4*, *Cd68*, and DAPI using IHC. (Scale bars: 50 μ m, *Left* and 20 μ m, magnification.) *SI Appendix, Fig. S11* shows additional corresponding stainings. (I) Sections as in D were stained for F4/80 and Cd169 (*Top*) or SIGIRR1 and Cd11b (*Bottom*) using IHC. (Scale bars: 50 μ m, *Left* and 20 μ m, magnification.) Arrows indicate costaining of all markers, asterisk indicates costain of the marker of interest with a known myeloid marker, and arrowheads indicate individual staining.

The Composition, Origin, and Phenotype of Nerve-Associated Myeloid Cells Is Unique. We next studied nerve-associated myeloid lineage cells using IHC and reporter mice. One myeloid lineage cluster (named MC) expressed *Cx3cr1* in mice. To confirm this population, we used CX3CR1-GFP reporter mice. We found that *Cx3cr1*-driven GFP was expressed by a proportion of endoneurial mononuclear cells (Fig. 3H and *SI Appendix*, Fig. S11). This population coexpressed Cd68, while it did not costain for *Cxcl4* (encoded by *Pf4*) by IHC. This indicated that one of two distinct subsets of nerve-associated macrophages can be identified by *Cx3cr1* and absence of *Cxcl4* (Fig. 3H and *SI Appendix*, Fig. S11).

Conversely, we found that another population of endoneurial cells coexpressed the *Cxcl4* protein (encoded by *Pf4*; MP cluster) and the myeloid marker Cd68 (Fig. 3H and *SI Appendix*, Fig. S11). *Cxcl4*-positive cells were located in close proximity to F4/80⁺ and Cd169⁺ macrophages, but did not coexpress these markers (Fig. 3I, *Top*). When we stained for more specific markers, we found that *Cxcl4*-expressing cells were positive for Cd11b and SIGNR1; both have been associated with pathogen recognition and phagocytosis in macrophages (40) (Fig. 3I, *Bottom*). This suggests that the *Cxcl4*-expressing MP cluster represents phagocytosing nerve-associated macrophages. Notably, *Cxcl4*-expressing macrophages were recently identified in CNS-associated border compartments of healthy mice (41). Overall, we thus identified the transcriptional profile of two subsets of nerve-associated myeloid cells characterized by expression of *Cx3cr1* (MC cluster) and *Pf4/Cxcl4* (MP cluster), respectively.

We next initially addressed the ontogenetic origin of nerve-associated myeloid cells. In an *Flt3Cre*-driven switch-reporter mouse, cells originating from yolk sac hematopoiesis (e.g., microglia) express tdTomato (tdT), while hematopoietic lineages derived from fetal liver and bone marrow express GFP (42) (*SI Appendix*, Fig. S12A). As expected, myeloid cells in the brain were mostly tdT⁺ (89.75%; i.e., yolk sac-derived microglia) and in other organs were >80% GFP⁺ (bone marrow 87.1% and spleen 81.9%; *SI Appendix*, Fig. S12B). In contrast, the PNS contained ~35% tdT⁺ myeloid cells (36.75%; *SI Appendix*, Fig. S12C and D) suggesting a partially late embryonic or bone marrow hematopoietic stem cell (HSC)-derived origin and supporting the heterogeneity of PNS myeloid cells.

Autoimmunity Induces Specific Compositional and Phenotypic Changes in PNS Cells. We next aimed to understand how autoimmunity shapes the composition and phenotype of PNS cells. We therefore extracted nerve cells from a mouse model of spontaneous chronic peripheral neuritis (43). We thereby generated single cell transcriptomes from PNS cells of young and clinically unaffected ICAM-1^{-/-} nonobese diabetic (NOD) mice (5,250 cells, *n* = 12 female mice) that histologically did not show PNS inflammation (*SI Appendix*, Fig. S13A) and of prediabetic NOD control mice (5,400 cells, *n* = 24 female mice). Although cell-type clustering clearly reidentified the PNS cell clusters we had identified in healthy mice (Fig. 4A and B and *SI Appendix*, Table S9), ICAM-1^{-/-}NOD nerves contained grossly expanded leukocyte clusters while parenchymal cells and myeloid lineage cells (MC/MP clusters) were underrepresented in comparison to NOD control mice (Fig. 4A and B). Due to their underrepresentation, the transcriptionally similar vSMC/PC and the MC/MP clusters no longer separated into distinct clusters, while plasmacytoid dendritic cells (pDCs) were identified in both genotypes (Fig. 4A and B) resulting in 11 total cell clusters. The presence of pDCs was not detected in other datasets and may thus be specific for the NOD genetic background.

The expanded clusters were mainly CD4-expressing T cells with a memory phenotype that previously has been described for tissue-resident memory TCs (CD4; *Vps37b*, *Cxcr6*, *Tnfrsf3*, and *Rora*) (44), and BCs with an activated phenotype (*H2-DMb2*/

MHC class II, *Ms4a1/Cd20*, *Cd83*, and *Cd74*). In addition, ICAM-1^{-/-}NOD nerves contained expanded clusters of cytotoxic CD8 TCs (CD8; *Cd8a*, *Klrc1*, and *Nkg7*), and pDCs (*Flt3* and *Siglech*) (*SI Appendix*, Fig. S13B and Table S9). Myeloid lineage cells (*Adgre1/F4/80* and *Pf4/Cxcl4*) were not numerically expanded, but showed a more activated phenotype with increased expression of *Cx3cr1* and costimulatory molecules like *Cd86* (MC cluster) (*SI Appendix*, Fig. S13B and Table S9). We confirmed this unique phenotype of PNS-infiltrating cells including the presence of pDCs by flow cytometry (Fig. 4C). PNS autoimmunity in ICAM-1^{-/-}NOD thus induces a local accumulation of specific leukocyte populations including memory and cytotoxic T cells and pDCs, while homeostatic nerve-associated macrophages are underrepresented.

We next aimed to construct an integrated view of how non-immune cell types respond to autoimmune tissue destruction. We first focused on vascular cells and identified a set of differentially expressed (DE) genes in vascular endothelial cells in ICAM-1^{-/-}NOD compared to NOD control cells (Fig. 4D and *SI Appendix*, Table S10). DE genes were characterized by the induction of a chemokine (*Ccl5*), antigen-presenting molecules (*B2m* and *H2-D1*), and signs of cellular stress (*mt-Co2*) (*SI Appendix*, Table S10). The neuritis-specific transcriptome in the nmSC (Fig. 4E and *SI Appendix*, Table S11) and mySC (Fig. 4F and *SI Appendix*, Table S12) clusters also featured an up-regulation of antigen-presenting molecules (*H2-K1*, *H2-D1*, and *B2m*) and immunoproteasome subunits (*Psmb8* and *Psmb10*) in line with the known conditional antigen-presenting function of Schwann cells (45) (*SI Appendix*, Fig. S13C). Both nmSCs and mySCs also down-regulated some of their cluster-defining transcripts, including collagen (*Col1a1*) (Fig. 4E) and myelin proteins (*Pmp22* and *Mpz*) (Fig. 4F), respectively. In contrast, mySCs from ICAM-1^{-/-}NOD mice up-regulated *Sostdc1* and *Zeb2* (*SI Appendix*, Table S12)—two transcripts previously identified to coregulate posttraumatic Schwann cell differentiation and nerve regeneration (46, 47). In summary, autoimmunity causes induction of immune-related transcripts, loss of structural parenchymal components, and signs of cellular dedifferentiation in the PNS.

We next analyzed whether the response of PNS tissue to autoimmunity was similar or distinct from the CNS. We therefore compared genes DE in the mySC cluster under neuritis conditions with genes DE in oligodendrocytes (oligos; myelinating glia of the CNS) in the experimental autoimmune encephalomyelitis (EAE) animal model of human multiple sclerosis (MS) (48). Using a similar threshold for significance (*Methods*), we found that 32 (15.4%) of 208 genes DE in mySCs were also DE in oligos in EAE (Fig. 4G and *SI Appendix*, Table S13). Notably, 30 (94%) of these 32 genes were canonical IFN-response genes (*SI Appendix*, Fig. S14). The transcriptional response of myelinating glia to autoimmunity is thus partially conserved between oligos and mySCs and mimics an IFN-dependent antiviral response.

Autoimmunity Diversifies Cell-Cell Communication in the Peripheral Nerve. We next aimed to identify mechanisms controlling intercellular communication in the PNS. We therefore systematically predicted intercellular signaling by adapting a recently described human tool (49) for mouse data (*Methods*). In these predicted networks, cell types are defined as nodes (circles) and ligand-receptor pairings predicted from expression data are defined as directional edges (arrows) (*SI Appendix*, Fig. S15A and C). The network of nondiseased NOD nerves showed high connectivity of leukocyte clusters (MCs, BCs, pDCs) and of the fibro and nmSC clusters (*SI Appendix*, Fig. S15A and B) as illustrated by the high number of edges (*SI Appendix*, Table S14). Multiple interactions were directed from EC1 to fibro and nmSC clusters (*SI Appendix*, Fig. S15A and B). Fewer edges originated

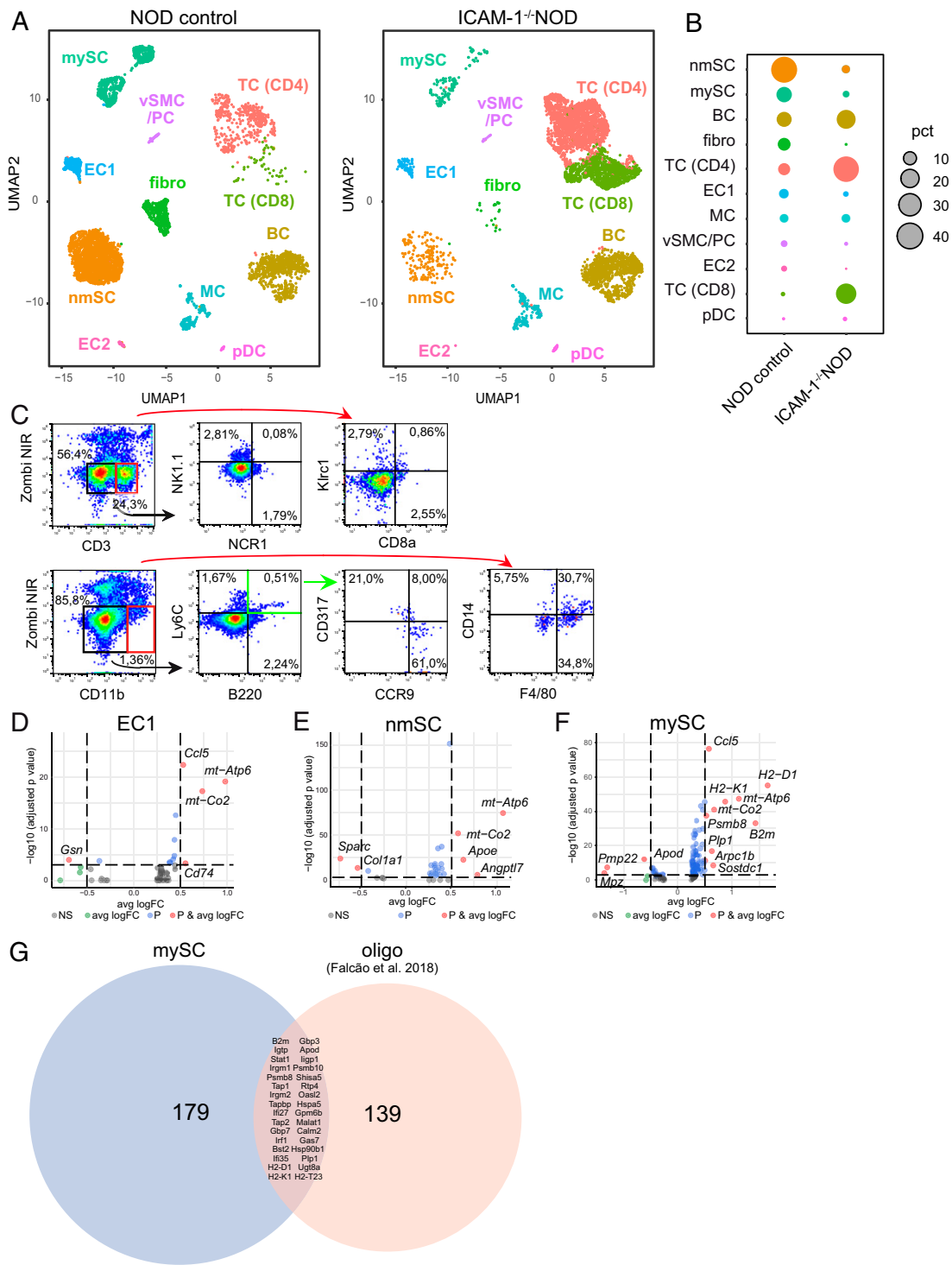


Fig. 4. Neuritis induces influx of lymphocytes and a partially shared autoimmunity module in myelinating Schwann cells. (A) Peripheral nerve cells were purified from female prediabetic NOD control mice (Left, $n = 24$ mice, two biological replicates) and ICAM-1^{-/-}NOD mice (Right, $n = 12$ mice, one biological replicate) and processed by scRNA-seq. The resulting NOD control ($n = 5,400$) and ICAM-1^{-/-}NOD ($n = 5,250$) sc transcriptomes were clustered and are shown in UMAP plots. (B) The percentage of cells in each cluster in NOD control and ICAM-1^{-/-}NOD samples is depicted in a dotplot with circle size representing proportion of cells in each cluster. (C) Peripheral nerve cells were purified from presymptomatic female ICAM-1^{-/-}NOD mice ($n = 5$) and characterized by flow cytometry. The proportion CD8⁺ cytotoxic T cells (Top Right) and NK1.1⁺NCR1⁺ NK cells (Top Middle) was quantified. B220⁺ B cells (Lower Middle Left), B220⁺Ly6C⁺CCR9⁺CD137⁺ plasmacytoid dendritic cells (Lower Middle Right), and CD11b⁺F4/80⁺CD14⁻ macrophages (Lower Far Right) was quantified. One out of two independent experiments is shown. (D–F) Volcano plots depicting DE genes between ICAM-1^{-/-}NOD vs. NOD control samples in endothelial cells (EC1) (D), nmSCs (E), and mySCs (F). Only DE genes with an average (avg) log fold change (FC) $> \pm 0.25$ are plotted. Genes with an avg log FC above ± 0.5 and P values < 0.001 are marked in red and the gene names are provided. The y axes represent the negative log₁₀ of the adjusted P value. (G) Venn diagram showing genes DE in ICAM-1^{-/-}NOD vs. NOD mice within mySC compared with DE genes within oligodendrocytes (oligo) in EAE vs. control samples in an available dataset (48). EC1: endothelial cells cluster 1, EC2: endothelial cells cluster 2, TC(CD4): CD4 T helper cells, TC(CD8): cytotoxic CD8 T cells and natural killer cells, NS: not significant, P: adjusted P value, pct: percentage expressed.

from the mySC cluster, suggesting low intercellular connectivity of mySCs in the uninflamed peripheral nerve.

We also applied the network analysis to neuritis and—as expected—found that leukocyte clusters increased in size and the total number of intercellular interactions increased in ICAM-1^{-/-}NOD nerves (edge count in *SI Appendix, Fig. S15 C and D* and *Table S14*). Surprisingly, the “betweenness centrality” as a measure of the amount of control that one node exerts over the interactions of other nodes (49), did not increase for most leukocyte clusters (MC, pDC, BC), but instead changed for fibro and vSMC/PC clusters (*SI Appendix, Table S14*). This suggests that fibro and vSMC/PC clusters gain more control over local cell–cell communication in autoimmunity. Comparative network analysis may thus help to prioritize candidate signaling pathways in disease.

Discussion

In this study, we generated an unbiased map of the cellular composition and transcriptional phenotype of PNS cells in health and autoimmunity. We identified and confirmed markers of nonmyelinating SCs and nerve-associated fibroblasts. Such cell-type-specific markers will likely facilitate better characterization of these cell types. We also found an unexpectedly diverse and unique leukocyte repertoire in the PNS with two subsets of nerve-associated homeostatic myeloid cells identified by specific gene sets. And chronic autoimmune neuritis induced an expansion of lymphocytes that altered the local cell signaling circuitry. Notably, the transcriptional tissue response to autoimmunity was partially shared between peripheral and central nervous system glia cells and resembled an IFN response. This suggests a degree of stereotypicality in the response of glia cells to autoimmunity.

We used a specific extraction protocol that was balanced for optimum cell viability at maximum yield and allows identifying all expected PNS cell types. This approach is useful to screen for subsets of PNS cells, but does not allow quantifying the absolute and relative cell abundance in the PNS as observed previously (6) in contrast to morphological approaches (7). For example, SCs are likely more difficult to extract than leukocytes and therefore seem underrepresented.

We found considerable transcriptional differences between mySCs and nmSCs. Although nmSCs clearly expressed SC lineage markers by transcriptomics, ISH, and IHC (Figs. 1*D* and 2*B* and *C*), this cluster expressed multiple transcripts (e.g., *Ccl11*), including a specific transcription factor (*Osr2*) that had not been previously associated with PNS glia cells. Interestingly, we also identified a number of genes that were previously associated with myelination, but showed the highest expression in nmSCs rather than mySCs (e.g., *Tcf4*, *Spry2*, and *Ebfl1*). These transcripts in nmSCs may indirectly affect myelination in mySCs. Overall, our findings suggest that nmSCs have previously been both numerically and functionally underappreciated in the PNS. In comparison to a recent study of the injured peripheral nerve (6), we profile a fourfold higher number of cells, validate marker genes, and focus on nerve-associated leukocytes.

Specifically, we identify two distinct subsets of nerve-associated myeloid cells, while lymphocytes increase in autoimmune neuritis (Fig. 4). Nerve-associated macrophages have been well documented (e.g., ref. 50) and may promote myelin loss in some genetically defined and age-related neuropathies (51, 52). However, their exact phenotype and function in the PNS are unknown (53). They are partly replenished from the blood within months and are partly long living and tissue resident (54) and proliferate locally in response to different types of injury (55–57). Endoneurial macrophages have been studied in traumatic nerve injury (58) and their recruitment to the PNS occurs early after nerve transection in nonmammals (59). We speculate that endoneurial *Pf4*-expressing vs. *Cx3cr1*-expressing macrophages

constitute PNS-resident myeloid lineage cells of different source and ontogenetic origin.

Except for *Aif1/Iba1*, we did not detect any recently established markers for microglia (e.g., *P2ry12*, *Tmem119*, *Sparc*, and *Olfm3*) (41, 60) in PNS-derived macrophages (*SI Appendix, Fig. S12D* and *Table S2*). Therefore, nerve-associated macrophages are likely transcriptionally distinct from microglia. In contrast to the known yolk-sac origin of microglia, nerve-associated macrophages also seem to have a mixed developmental origin with bone marrow-derived hematopoietic progenitors partially contributing to this population. In conclusion, our study opens diverse avenues for better understanding the PNS.

Methods

Animals. C57BL/6J, *Icam1*^{tm1Jcgr1}NOD (named ICAM-1^{-/-}NOD for simplicity), NOD/ShiLtJ, CX3CR1-GFP, hGFAP-GFP, PDGFR α -EGFP, and Flt3Cre-mT/mG mice and Lewis rats were used. Mice were without signs of neuropathy (ICAM-1^{-/-}NOD) or diabetes (NOD/ShiLtJ).

Cell Extraction and Purification. Sciatic nerves and the brachial nerve plexus were dissected from intracardially phosphate buffered saline (PBS)-perfused animals and finely chopped. Enzymatic digestion was optimized (*SI Appendix, SI Material and Methods*) and adapted from a previous study (61). Myelin was depleted using anti-myelin beads (Miltenyi Biotec). Single cells were subsequently sorted (BD FACSAria III) for intact viable cells using three viability markers: Zombi NIR APC Cy7, Calcein-AM FITC, and DAPI (Biolegend) (*SI Appendix, Fig. S1*).

Single Cell RNA-Sequencing and Analysis. Single cell RNA-sequencing was performed using the Chromium Single Cell 3' Kit with v2 chemistry (10x Genomics) according to manufacturer instructions. Sequencing was done either on a local Illumina Nextseq500 (High-Through 75 Cycle Kit) with a 26-8-0-57 read setup or commercially on a NovaSeq6000 (300 Cycle Kit) with paired end 150 read setup. Details are provided in *SI Appendix, Table S1*.

Processing of raw sequencing data was performed with the *cellranger* pipeline v3.0.2. Subsequent analysis steps were carried out with the R-package *Seurat* v3.0.0 (62) using R v3.6.0 as recommended. Unique molecular identifier (UMI) data were normalized using an approach with regularized negative binomial regression (63). Dimensionality reduction was done by uniform manifold approximation and projection (UMAP) with default parameters. DE genes were identified with “FindMarkers” function in *Seurat*. The threshold was set to 0.25 average log fold change and using Wilcoxon rank sum test, unless otherwise stated. To annotate the clusters, genes differentially expressed in a one vs. all cluster comparison were queried for known expression in a literature search and plotted in feature plots.

DE genes were identified between ICAM-1^{-/-}NOD and NOD conditions after alignment using *Harmony* (64). Interactions between the cells were predicted using CellPhoneDB (49) with normalized and filtered scRNA-seq and conversion of murine ensembl IDs to human using biomaRt. Statistical significance of the cellular interactions were calculated as described (49). Interactions between clusters were visualized in a heatmap and clustered with complete linkage and Euclidean distance measure using the R package *pheatmap*. Network visualization was performed with Cytoscape v.3.7.1 and GSEA with the *Enrichr* tool.

Comparison with Published Datasets. We compared DE genes in ICAM-1^{-/-}NOD vs. NOD control mice in specific clusters with a published dataset of DE genes in EAE vs. control mice (48). To improve comparability, DE genes in our dataset were identified using MAST instead of Wilcoxon rank sum test with a lower average log fold change of 0.095. All DE genes with an adjusted *P* value greater than 0.05 were removed. The top up- and down-regulated DE genes of the Falcao dataset (48) (cutoff gene expression > |4|) were compared with our top DE genes using the *VennDiagram* package) (*SI Appendix, Table S13*). Intersecting genes were then analyzed using the “Interferome” database.

Immunohistochemistry. Fixed frozen slides were used for histology-based methods. Slides were stained with Cd68, F4/80, Cxcl4, Cd169, Cd11b, and SIGNR1. Secondary Alexa Fluor (AF)-conjugated antibodies were used. Slides were mounted in Fluoromount G with DAPI (Invitrogen). Images were taken using a three laser fluorescent microscope (Bioevo BZ-900 microscope with BZII Viewer software, Keyence) and processed in ImageJ.

Five total human samples were selected according to lack of pathological findings in sural nerve biopsies. The study received ethical approval by the ethical board of the University Clinic Leipzig, Germany. The staining was performed by the automated immunostainer Benchmark XT (Roche). The following antibodies were used: CD45, CD68, CD8, CD4, CD34, SMA/ACTA2, SOX10, and MBP.

RNA in situ hybridization. RNA ISH was performed on fixed/fresh frozen and paraffin-embedded sections of sciatic nerves from intracardial PBS-perfused C57BL/6 mice, hGFAP-GFP mice, and PDGFR α -EGFP mice. Three different ISH kits were used according to manufacturer protocol. The Thermo Fisher ViewRNA ISH Tissue Assay Kit (1-plex) was used to detect Mm-Mbp, Mm-Apod, Mm-Smoc2, Mm-Sfrp4, and Mm-Pf4 as single stains. The Thermo Fisher ViewRNA Cell Assay Kit (multiplex) was used, in combination with the first steps of the previously mentioned tissue assay kit, to detect Mm-Apod, Mm-Smoc2, Mm-Ngfr, Mm-S100b, Mm-Sox10, Mm-Sfrp4, and Mm-Pit16 in different single and costain settings. The ACDBio BaseScope Detection Reagent Kit-RED (1-plex) was used to detect Mm-Smoc2 and Mm-Sfrp4 in costain with antibodies for Mbp. All images were obtained with an Axio Observer Z1 (Zeiss) and processed in AxioVision and ImageJ.

Flow Cytometry of Leukocytes. Flow cytometry analysis was performed on isolated PNS cells. The following viability dye and murine antibodies were

used: Zombie NIR, CD45, CD11b, B220, CD3, CD4, CD8, NK1.1, NKG2AB6, NKp46, F4/80, CD14, Ly6C, CD317, CCR9, CD11c, and MHCII. Samples were measured on the Gallios (10 colors, 3 lasers, Beckman Coulter) and analyzed with FlowJo_V10.

Data Availability. The raw scRNA-seq data supporting the findings in this study have been deposited in the GEO repository with the accession code GSE142541, available at <https://www.ncbi.nlm.nih.gov/geo/query/acc.cgi?acc=GSE142541>. All processed scRNA-seq data are included as **Datasets S1–S14**. Additional figures supporting the main text, are provided in **SI Appendix**.

A full overview of the methods can be found in **SI Appendix**.

ACKNOWLEDGMENTS. We thank Dr. Antonio Castrillo, Universidad Autónoma de Madrid, Madrid, Spain for providing us with the Cd169 antibody. C.S. was supported by the Deutsche Forschungsgemeinschaft (DFG) Sonderforschungsbereich 914, project A10. G.M.z.H. was supported by grants from the DFG (ME4050/4-1 and ME4050/8-1), from the Innovative Medical Research program of the University Münster, and from the Ministerium für Innovation, Wissenschaft und Forschung of the state Nordrhein-Westfalen. This project was funded in part by the DFG Sonderforschungsbereich Transregio 128 (to H.W.).

1. J. L. Salzer, Schwann cell myelination. *Cold Spring Harb. Perspect. Biol.* **7**, a020529 (2015).
2. K. A. Nave, H. B. Werner, Myelination of the nervous system: Mechanisms and functions. *Annu. Rev. Cell Dev. Biol.* **30**, 503–533 (2014).
3. L. Richard *et al.*, Endoneurial fibroblast-like cells. *J. Neuropathol. Exp. Neurol.* **71**, 938–947 (2012).
4. E. Ydens *et al.*, The neuroinflammatory role of Schwann cells in disease. *Neurobiol. Dis.* **55**, 95–103 (2013).
5. G. Meyer zu Hörste, W. Hu, H. P. Hartung, H. C. Lehmann, B. C. Kieseier, The immunocompetence of Schwann cells. *Muscle Nerve* **37**, 3–13 (2008).
6. M. J. Carr *et al.*, Mesenchymal precursor cells in adult nerves contribute to mammalian tissue repair and regeneration. *Cell Stem Cell* **24**, 240–256.e9 (2019).
7. S. Stierli *et al.*, The regulation of the homeostasis and regeneration of peripheral nerve is distinct from the CNS and independent of a stem cell population. *Development* **145**, dev170316 (2018).
8. T. Xie *et al.*, Single-cell deconvolution of fibroblast heterogeneity in mouse pulmonary fibrosis. *Cell Rep.* **22**, 3625–3640 (2018).
9. G. X. Zheng *et al.*, Massively parallel digital transcriptional profiling of single cells. *Nat. Commun.* **8**, 14049 (2017).
10. M. Vanlandewijck *et al.*, A molecular atlas of cell types and zonation in the brain vasculature. *Nature* **554**, 475–480 (2018).
11. E. A. Winkler, R. D. Bell, B. V. Zlokovic, Central nervous system pericytes in health and disease. *Nat. Neurosci.* **14**, 1398–1405 (2011).
12. A. K. Reinhold, J. Schwabe, T. J. Lux, E. Salvador, H. L. Rittner, Quantitative and microstructural changes of the blood-nerve barrier in peripheral neuropathy. *Front. Neurosci.* **12**, 936 (2018).
13. E. F. Lim *et al.*, AlphaB-crystallin regulates remyelination after peripheral nerve injury. *Proc. Natl. Acad. Sci. U.S.A.* **114**, E1707–E1716 (2017).
14. S. M. Fullerton, W. J. Strittmatter, W. D. Matthews, Peripheral sensory nerve defects in apolipoprotein E knockout mice. *Exp. Neurol.* **153**, 156–163 (1998).
15. E. I. Girolami, D. Bouhy, M. Haber, H. Johnson, S. David, Differential expression and potential role of SOCS1 and SOCS3 in Wallerian degeneration in injured peripheral nerve. *Exp. Neurol.* **223**, 173–182 (2010).
16. D. B. Parkinson *et al.*, c-Jun is a negative regulator of myelination. *J. Cell Biol.* **181**, 625–637 (2008).
17. C. L. Blom, L. B. Mårtensson, L. B. Dahlin, Nerve injury-induced c-Jun activation in Schwann cells is JNK independent. *BioMed Res. Int.* **2014**, 392971 (2014).
18. S. Levi, C. Taveggia, Iron homeostasis in peripheral nervous system, still a black box? *Antioxid. Redox Signal.* **21**, 634–648 (2014).
19. P. Spreyer *et al.*, Regeneration-associated high level expression of apolipoprotein D mRNA in endoneurial fibroblasts of peripheral nerve. *EMBO J.* **9**, 2479–2484 (1990).
20. M. H. G. Verheijen, R. Christ, P. Burrola, G. Lemke, Local regulation of fat metabolism in peripheral nerves. *Genes Dev.* **17**, 2450–2464 (2003).
21. N. García-Mateo *et al.*, Schwann cell-derived Apolipoprotein D controls the dynamics of post-injury myelin recognition and degradation. *Front. Cell. Neurosci.* **8**, 374 (2014).
22. M. D. Ganfornina *et al.*, Apod, a glia-derived apolipoprotein, is required for peripheral nerve functional integrity and a timely response to injury. *Glia* **58**, 1320–1334 (2010).
23. J. L. Salzer, L. Lovejoy, M. C. Linder, C. Rosen, Ran-2, a glial lineage marker, is a GPI-anchored form of ceruloplasmin. *J. Neurosci. Res.* **54**, 147–157 (1998).
24. D. Malin *et al.*, The extracellular-matrix protein matrilin 2 participates in peripheral nerve regeneration. *J. Cell Sci.* **122**, 995–1004 (2009). Correction in: *J. Cell Sci.* **122**, 1471 (2009).
25. H. S. Kwon *et al.*, Myocilin mediates myelination in the peripheral nervous system through ErbB2/3 signaling. *J. Biol. Chem.* **288**, 26357–26371 (2013).
26. C. Colombelli *et al.*, Perlecan is recruited by dystroglycan to nodes of Ranvier and binds the clustering molecule gliomedin. *J. Cell Biol.* **208**, 313–329 (2015).
27. P. Vitale, P. Braghetta, D. Volpin, P. Bonaldo, G. M. Bressan, Mechanisms of transcriptional activation of the col6a1 gene during Schwann cell differentiation. *Mech. Dev.* **102**, 145–156 (2001).
28. C. Lopez-Anido *et al.*, Differential Sox10 genomic occupancy in myelinating glia. *Glia* **63**, 1897–1914 (2015).
29. B. Hausott, L. Klimaschewski, Sprouty2-a novel therapeutic target in the nervous system? *Mol. Neurobiol.* **56**, 3897–3903 (2019).
30. J. A. Cox, B. Zhang, H. M. Pope, M. M. Voigt, Transcriptome analysis of chemically-induced sensory neuron ablation in Zebrafish. *PLoS One* **11**, e0148726 (2016).
31. S. Maysami *et al.*, Oligodendrocyte precursor cells express a functional chemokine receptor CCR3: Implications for myelination. *J. Neuroimmunol.* **178**, 17–23 (2006).
32. S. Stricker *et al.*, Odd-skipped related genes regulate differentiation of embryonic limb mesenchyme and bone marrow mesenchymal stromal cells. *Stem Cells Dev.* **21**, 623–633 (2012).
33. L. Marvaldi *et al.*, Enhanced axon outgrowth and improved long-distance axon regeneration in sprouty2 deficient mice. *Dev. Neurobiol.* **75**, 217–231 (2015).
34. D. Moruzzo *et al.*, The transcription factors EBF1 and EBF2 are positive regulators of myelination in Schwann cells. *Mol. Neurobiol.* **54**, 8117–8127 (2017).
35. C.-J. Liang *et al.*, SFRPs are biphasic modulators of Wnt-signaling-elicited cancer stem cell properties beyond extracellular control. *Cell Rep.* **7**, 12904 (2017).
36. S. L. Peterson, H. X. Nguyen, O. A. Mendez, A. J. Anderson, Complement protein C3 suppresses axon growth and promotes neuron loss. *Sci. Rep.* **7**, 12904 (2017).
37. S. Chakarov *et al.*, Two distinct interstitial macrophage populations coexist across tissues in specific subtissular niches. *Science* **363**, eaau0964 (2019).
38. Y. Wolf, S. Yona, K.-W. Kim, S. Jung, Microglia, seen from the CX3CR1 angle. *Front. Cell. Neurosci.* **7**, 26 (2013).
39. F. Pertuy *et al.*, Broader expression of the mouse platelet factor 4-cre transgene beyond the megakaryocyte lineage. *J. Thromb. Haemost.* **13**, 115–125 (2015).
40. Y. Kawauchi *et al.*, SIGNR1-mediated phagocytosis, but not SIGNR1-mediated endocytosis or cell adhesion, suppresses LPS-induced secretion of IL-6 from murine macrophages. *Cytokine* **71**, 45–53 (2015).
41. M. J. C. Jordão *et al.*, Single-cell profiling identifies myeloid cell subsets with distinct fates during neuroinflammation. *Science* **363**, eaat7554 (2019).
42. E. Gomez Perdiguero *et al.*, Tissue-resident macrophages originate from yolk-sac-derived erythro-myeloid progenitors. *Nature* **518**, 547–551 (2015).
43. G. Meyer zu Horste *et al.*, Thymic epithelium determines a spontaneous chronic neuritis in Icam1(tm1Jcgr)NOD mice. *J. Immunol.* **193**, 2678–2690 (2014).
44. R. J. Miragaia *et al.*, Single-cell transcriptomics of regulatory T cells reveals trajectories of tissue adaptation. *Immunity* **50**, 493–504.e7 (2019).
45. M. Hartlehnert *et al.*, Schwann cells promote post-traumatic nerve inflammation and neuropathic pain through MHC class II. *Sci. Rep.* **7**, 12518 (2017).
46. D. Schmid, T. Zeis, N. Schaeren-Wiemers, Transcriptional regulation induced by cAMP elevation in mouse Schwann cells. *ASN Neuro* **6**, 137–157 (2014).
47. S. Quintes *et al.*, Zeb2 is essential for Schwann cell differentiation, myelination and nerve repair. *Nat. Neurosci.* **19**, 1050–1059 (2016).
48. A. M. Falcão *et al.*, Disease-specific oligodendrocyte lineage cells arise in multiple sclerosis. *Nat. Med.* **24**, 1837–1844 (2018).
49. R. Vento-Tormo *et al.*, Single-cell reconstruction of the early maternal-fetal interface in humans. *Nature* **563**, 347–353 (2018).
50. J. W. Griffin *et al.*, Macrophage responses and myelin clearance during Wallerian degeneration: Relevance to immune-mediated demyelination. *J. Neuroimmunol.* **40**, 153–165 (1992).
51. D. Klein *et al.*, Targeting the colony stimulating factor 1 receptor alleviates two forms of Charcot-Marie-Tooth disease in mice. *Brain* **138**, 3193–3205 (2015).

52. X. Yuan *et al.*, Macrophage depletion ameliorates peripheral neuropathy in aging mice. *J. Neurosci.* **38**, 4610–4620 (2018).
53. E. Ydens *et al.*, Acute injury in the peripheral nervous system triggers an alternative macrophage response. *J. Neuroinflammation* **9**, 176 (2012).
54. M. Müller, C. Leonhard, M. Krauthausen, K. Wacker, R. Kiefer, On the longevity of resident endoneurial macrophages in the peripheral nervous system: A study of physiological macrophage turnover in bone marrow chimeric mice. *J. Peripher. Nerv. Syst.* **15**, 357–365 (2010).
55. M. Mäurer *et al.*, Origin of pathogenic macrophages and endoneurial fibroblast-like cells in an animal model of inherited neuropathy. *Mol. Cell. Neurosci.* **23**, 351–359 (2003).
56. M. Mueller *et al.*, Macrophage response to peripheral nerve injury: The quantitative contribution of resident and hematogenous macrophages. *Lab. Invest.* **83**, 175–185 (2003).
57. M. Müller *et al.*, Contribution of resident endoneurial macrophages to the local cellular response in experimental autoimmune neuritis. *J. Neuropathol. Exp. Neurol.* **65**, 499–507 (2006).
58. M. Mueller *et al.*, Rapid response of identified resident endoneurial macrophages to nerve injury. *Am. J. Pathol.* **159**, 2187–2197 (2001).
59. A. F. Rosenberg, M. A. Wolman, C. Franzini-Armstrong, M. Granato, In vivo nerve-macrophage interactions following peripheral nerve injury. *J. Neurosci.* **32**, 3898–3909 (2012).
60. M. Prinz, D. Erny, N. Hagemeyer, Ontogeny and homeostasis of CNS myeloid cells. *Nat. Immunol.* **18**, 385–392 (2017).
61. M. P. Clements *et al.*, The wound microenvironment reprograms Schwann cells to invasive mesenchymal-like cells to drive peripheral nerve regeneration. *Neuron* **96**, 98–114.e7 (2017).
62. A. Butler, P. Hoffman, P. Smibert, E. Papalexi, R. Satija, Integrating single-cell transcriptomic data across different conditions, technologies, and species. *Nat. Biotechnol.* **36**, 411–420 (2018).
63. C. Hafemeister, R. Satija, Normalization and variance stabilization of single-cell RNA-seq data using regularized negative binomial regression. *Genome Biol.* **20**, 296 (2019).
64. I. Korsunsky *et al.*, Fast, sensitive and accurate integration of single-cell data with Harmony. *Nat. Methods* **16**, 1289–1296 (2019).